Enhanced Subpixel Mapping With Spatial Distribution Patterns of Geographical Objects

Yong Ge, *Member, IEEE*, Yuehong Chen, Alfred Stein, Sanping Li, and Jianlong Hu

***Abstract*—This paper proposes spatial distribution pattern-based subpixel mapping (SPM_S) as a novel subpixel mapping (SPM) strategy. It separately considers spatial distribution patterns of different types of geographical objects. Initially, it classifies geographical objects into areal, linear, and point patterns according to their spatially geometric characteristics. For the different patterns, SPM_S uses the vectorial boundary-based SPM algorithm with the spatial dependence assumption to deal with areal objects, the linear template matching-based SPM algorithm for linear objects, and the spatial pattern consistency matching-based SPM algorithm for point objects. The three patterns are integrated to generate a subpixel map. An artificially created image and two remotely sensed images were used to evaluate the performance of SPM_S. The results were compared with a traditional hard classifier and seven existing SPM methods. The experimental results demonstrated that SPM_S performed better than the hard classification and traditional SPM methods, particularly when dealing with linear and point objects.**

***Index Terms*—Classification, mixed pixel, remotely sensed images, spatial distribution patterns of geographical objects, subpixel mapping (SPM).**

I. Introduction

SUBPIXEL mapping (SPM) was introduced by Atkinson [1] to determine where the relative proportions of a class are within each pixel. Since then, much effort has been directed toward developing more efficient and accurate methods. These methods include pixel-swapping [2], linear optimization techniques [3]–[5], subpixel/pixel spatial attraction models [4], [6], Markov random fields [7]–[10], indicator cokriging [11]–[13], the geometric method [14], [15], the spatial regularization [16], [17] and artificial-intelligence-based methods such as differential evolution, an artificial immune system, and maximum *a posteriori* models [18]–[23]. They have been mainly developed under the spatial dependence assumption both within and between pixels and are applicable in high resolution (H-resolution), where pixels are smaller than the objects of interest [24] because they maximize the spatial dependence under the constraints of class proportions derived from soft classifications [25]. These methods, however, cannot effectively deal with low resolution (L-resolution), where the pixels are larger than the objects of interest [24], or with linear objects, where the pixels are both shorter and wider than the objects of interest [18]. Applying these methods in L-resolution, for instance, may result into clustering of objects, thus leading to a loss of the original characteristics, such as randomness or dispersion [24]. In addition, applying them to fine linear objects may result into a loss of linear connectivity, whereas for large linear objects, it may lead to unsmooth boundaries [18]. Important in this respect is that these methods treat all objects as a single type when predicting their land cover classes.

To date, most SPM methods focus on predicting the spatial distribution in H-resolution. Lechner *et al.* [26] highlighted the requirement of SPM for mapping L-resolution and linear land cover objects for the representation of ecological values for natural resource management. Few studies, though, have addressed SPM for L-resolution and for linear objects. Tatem *et al.* [27] proposed the Hopfield neural network and Atkinson [28] proposed the two-point histogram to obtain the spatial distribution in L-resolution by incorporating prior information. Both methods provided acceptable solutions in predicting the land cover pattern of L-resolution objects at the subpixel scale [27], [28]. Such prior information, however, is typically in the form of finer training images and is either not readily available or requires laborious preprocessing [12]. To deal with linear objects, Ai *et al.* [29] used mathematical morphology to extract their central line from fraction images, which was used as auxiliary information to improve the accuracy using spatial annealing. Thornton *et al.* [30] added anisotropic modeling to pixel swapping to enhance the prediction of linear objects within the superresolution output. This modification resulted in an increase in the accuracy of mapping fine rectilinear objects as compared with pixel swapping [30], but ignored curvilinear objects [30].

To address these problems, this paper proposes a new SPM strategy called spatial distribution pattern-based SPM (SPM_S). SPM_S separately considers the spatial characteristics of land cover objects and recognizes geographical objects as having an

Manuscript received September 22, 2014; revised April 29, 2015 and October 2, 2015; accepted November 7, 2015. Date of publication January 14, 2016; date of current version March 9, 2016. This work was supported in part by the National Natural Science Foundation of China under Grant 41471296 and in part by the Key Technologies Research and Development Program of China under Grant 2012BAH33B01.

Y. Ge is with the State Key Laboratory of Resources and Environmental Information System, Institute of Geographical Sciences and Natural Resources Research, Chinese Academy of Sciences, Beijing 100101, China, and also with Jiangsu Center for Collaborative Innovation in Geographical Information Resource Development and Application, Nanjing 210023, China (e-mail: gey@lreis.ac.cn).

Y. Chen is with the State Key Laboratory of Resources and Environmental Information System, Institute of Geographical Sciences and Natural Resources Research, University of Chinese Academy of Sciences, Beijing 100101, China (e-mail: chenyh@lreis.ac.cn).

A. Stein is with the ITC International Institute for Geo-Information Science and Earth Observation, University of Twente, 7500 Enschede, The Netherlands (e-mail: a.stein@utwente.nl).

S. Li is with the Office of the CTO and EMC Labs China, EMC Corporation, Beijing 100027, China (e-mail: izhilong@hotmail.com).

J. Hu is with the School of Computer and Information Technology, Shanxi University, Taiyuan 030006, China (e-mail: weilong@sxu.edu.cn).

Color versions of one or more of the figures in this paper are available online at http://ieeexplore.ieee.org.

Digital Object Identifier 10.1109/TGRS.2015.2499790

areal pattern (A), a linear pattern (L), or a point pattern (P). The reason is that geographical objects are usually represented by these three patterns in a geographical information system (GIS) [31] according to their spatially geometric characteristics [24], [27], [29], [30]. A-objects corresponding to H-resolution cases are characterized by the spatial distribution of a large patch. Similarly, P-objects corresponding to L-resolution cases are scattered inside or on the edge of pixels and are represented as points within pixels. L-objects have linear shapes, for example, roads and rivers extending over several pixels. SPM_S considers A-objects using the vector boundary-based SPM (SPM_V) algorithm [15], which also uses the spatial dependence assumption and deals with A-objects. For L-objects, we develop the linear template matching-based SPM (SPM_L) algorithm, whereas for P-objects, we propose the spatial pattern consistency matching-based SPM (SPM_SP) algorithm. By using this strategy, SPM_S avoids various shortcomings. An artificially created test image and two remote sensing images are used to evaluate the effectiveness and performance of SPM_S.

The remainder of this paper is organized as follows. Section II briefly describes the background of SPM. Section III introduces the proposed SPM_S strategy. Section IV contains the experimental results and analysis. Section V presents the discussion. Section VI presents the conclusion.

II. Background

The aim of SPM is to determine appropriate locations of subpixels within a mixed pixel under the conditions of maximal spatial dependence and fixed fractions of land cover classes. Spatial dependence in SPM indicates that labels of neighboring pixels/subpixels are more likely to have the same land cover class than those farther apart [1].

Let C be the number of classes and suppose that C fraction images have been derived from coarse remotely sensed images, e.g., using a soft classification. Given the scale factor S, each pixel in the coarse image is divided into $S \times S$ smaller subpixels. Each subpixel is allocated a value 1 or 0 for each class, where the value 1 indicates that the subpixel belongs to the particular class, and the value 0 indicates otherwise.

Atkinson [24] classified SPM into two categories: regression-type and spatial optimization-type methods. In this paper, we describe the SPM as a linear optimization problem [3]. The objective is to maximize the spatial dependence of subpixels within a pixel, subject to constraints that each subpixel should be allocated to a single class and that the fraction of subpixels in each class is the same as the class fractions obtained from the classification. That is

$$\max \quad z = \sum_{c=1}^{C} \sum_{i=1}^{S^2} x_{ic} \times G_{ic} \tag{1}$$

$$\text{subject to} \begin{cases} \sum_{c=1}^{C} x_{ic} = 1 \\ \sum_{i=1}^{S^2} x_{ic} = F_{jc} \times S^2 \end{cases} \tag{2}$$

where G_{ic} is the spatial dependence measurement of class c in subpixel i, and F_{jc} is the fraction value of class c in mixed pixel j.

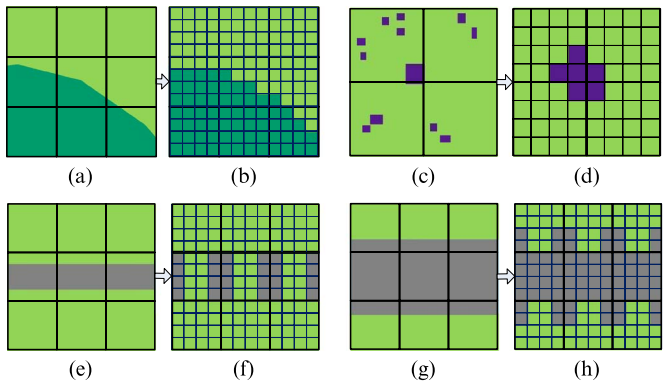

Fig. 1. SPM with spatial dependence theory. (a), (c), (e), and (g) Examples of A-, P-, and L-objects, respectively. (b) SPM for A-objects in (a). (d) SPM for P-objects in (c). (f) SPM for fine L-objects in (e). (h) SPM for larger L-objects in (g).

To predict the spatial distribution of different types of objects, we distinguish areal (A), linear (L), and point (P) patterns. Examples of A-, P-, and L-objects are shown in Fig. 1(a), (c), (e), and (g), where, for a scale factor $S = 4$, each coarse pixel consists of 16 smaller subpixels. Prediction of the spatial distribution of the A-objects in Fig. 1(a) is shown in Fig. 1(b) using (1). Spatial dependence states that neighboring pixels/subpixels are more likely to be the same than those farther apart [1]. Fig. 1(d) shows the prediction of P-objects in Fig. 1(c). These are commonly predicted to be the spatial distribution of aggregation. The P-objects within four neighboring pixels in Fig. 1(c) are predicted together at the central part of the four pixels in Fig. 1(d). Fig. 1(e) and (f) shows the prediction of L-objects. For those, connectivity is not retained when maximizing the spatial dependence of the fine linear objects. Maximizing the spatial dependence of the larger linear objects causes unsmooth boundaries, as shown in Fig. 1(g) and (h).

III. SPM_S

To identify geographic objects as A-, L-, and P-objects, we provide quantitative definitions in Section III-A. We use these patterns to illustrate the use of SPM_S for estimating their spatial distribution at the subpixel scale. It includes five main steps: spatial pattern recognition of objects, SPM for L-objects, SPM for A-objects, SPM for P-objects, and integration of the SPM results. Step 1 recognizes and partitions objects into A-, P-, and L-objects using the shape–density index [32] of each object as extracted from each fraction image by a seeded region-growing algorithm [33]. SPM_V [15], SPM_L, and SPM_SP are then used in steps 2, 3, and 4, respectively. Note that pure pixels are directly divided into subpixels by allocating the same class when the spatial locations of the objects are determined, whereas a decay function as used in SPM_V [15] provides the missing neighboring information of pixels in the image boundary region for mapping. Finally, the resulting patterns of the A-, L-, and P-objects are integrated into a single land cover map at a finer resolution with the fraction images. Details of the five steps of the SPM_S framework are described in the following.

A. Spatial Pattern Recognition of Objects

Step 1 starts with segmenting an image and extracting all pixels above a predefined fraction value in each fraction image using the seeded region-growing model (SRGM) [33]. In SRGM, pixel values within regions are considered to be similar, and it segments targets with similar characteristics and a similar connectivity [33]. SRGM has been successfully used to extract L-objects from remotely sensed images [32]. Next, the shape–density index [32] of each extracted object is computed to distinguish A- and L-objects from P-objects. After extracting A- and L-objects, the remaining pixels that have a smaller fraction value are identified as P-objects as they typically lie within a pixel and occupy a small area of the pixel [24], [27], [34]. The two main parts are as follows.

1) Segmenting and Extracting Objects: Segmentation by SRGM is defined as a partition of all pixels V into g separate nonempty regions $\{R_i | i = 1, 2, \ldots, g\}$. It is based on the following conditions [33].

1) Each region R_i consists of contiguous pixels.
2) $\cup_{i=1}^{g} R_i = \boldsymbol{V}$.
3) All pixels in R_i have the same properties, which are different from those of the pixels in its neighboring region $(R_j, i \neq j)$.

Before using SRGM to extract objects from fraction images, two homogeneity parameters and seeds are chosen. The homogeneity criterion [35] states that a pixel is added to a region if its fraction value during growing region exceeds a predetermined threshold ε, which determines if a pixel belongs to the object. The threshold is defined as $\varepsilon = \alpha/S$, where α is a parameter that is used as a balance to separate objects with larger fraction values (such as A- and L-objects) from objects with smaller fraction values (such as P-objects). In order to extract objects with relatively large fraction values (A- and L-objects), we set ε in this study to the empirical value $1/S$, which is required for L-objects to maintain connectivity [30]. Seeds $\{v_{jc} | j = 1, 2, \ldots, g\}$ indicate the coordinates of randomly selected pixels from the cth fraction image. Hence, a set of initial regions $\{R_{jc} | j = 1, 2, \ldots, g\}$ is created for the cth fraction image, and each region contains one pixel (the "seed"). This is followed by expanding the region R_{jc} from the start pixel by comparing the fraction values of its neighboring pixels with the predefined threshold ε. A neighboring pixel is included in the region if its fraction value exceeds the threshold ε. This is repeated until all the pixels in each fraction image have been considered, or the region cannot grow further. As a result, a set of g' final regions $\{R_{jc} | j = 1, 2, \ldots, g'\}$ is obtained.

2) Pattern Determination: The shape–density index [32] of each extracted region is calculated using

$$\begin{aligned} SD &= \omega_1 \cdot S + \omega_2 / D \\ S &= \frac{E}{(4 \cdot \sqrt{O})} \\ D &= \frac{N}{M} \end{aligned} \tag{3}$$

where S is the shape index, E is the perimeter of an object calculated by counting the boundary pixels of the region, O is the area of an object computed by counting the number of pixels inside the region, D is the density of an object in its bounding rectangle, N is the number of pixels in an object, M is the number of pixels in the bounding rectangle of an object, and ω_1, ω_2 are weights with $\omega_1 + \omega_2 = 1$. The regions are then classified as L- or A-objects according to a criterion in [32] that an object is considered as an L-object if $S \geq 2.3$, $D \leq 1.1$, and $SD \geq 1.6$; otherwise, the object is an A-object. Note that the criterion is slightly tuned to the needs of different remote sensing images and objects.

After determining L- and A-objects in each fraction image, the remaining pixels with fraction values greater than $1/S^2$ are P-objects as the area of a subpixel is equal to $1/S^2$ [5]. This way, for each fraction image, all pixels are identified as L-, A-, or P-objects $\dot{\boldsymbol{V}}_c = \{\boldsymbol{V}_c^L, \boldsymbol{V}_c^A, \boldsymbol{V}_c^P\}$, $c = 1, 2, \ldots, C$, and are used in the subsequent SPM processes.

B. SPM for L-Objects (SPM$_L$)

The second step concerns SPM$_\mathrm{L}$, i.e., SPM for L-objects. SPM$_\mathrm{L}$ relies on finding the optimal template for representing the direction of an L-object inside a mixed pixel. After determining the optimal template, the spatial distribution of the L-object is predicted using the fraction value constraints. There are three main parts: defining linear templates, matching linear templates, and SPM for L-objects.

1) Defining the Linear Templates: Different sizes of linear templates have been designed for mapping linear objects from remote sensing images. For example, Thornton *et al.* [30] used four rectilinear templates of 3×3 pixels and eight rectilinear templates of 5×5 pixels. In theory, templates can be designed for any size. To facilitate representing all occurrences of linear shape, we use linear 20 templates of 3×3 pixels, including rectilinear and curvilinear shapes (see Fig. 2). Compared with [30], which focused on four rectilinear directions (i.e., 0°, 45°, 90°, and 135°), the 20 templates in Fig. 2 represent rectilinear and curvilinear shapes and thus are useful when determining the appropriate direction for L-objects of various shapes. The templates are represented by a binary matrix

$$T_k = \begin{bmatrix} t(-1,-1) & t(-1,0) & t(-1,1) \\ t(0,-1) & t(0,0) & t(0,1) \\ t(1,-1) & t(1,0) & t(1,1) \end{bmatrix}, \quad k = 1, 2, \ldots, 20 \tag{4}$$

where $T_k = [t(m,n) \in \{1, 0\} | m, n = -1, 0, 1]$. The elements $t(m,n) = 1$ (see gray pixels in Fig. 2) represent the template, and the elements $t(m,n) = 0$ (see white pixels in Fig. 2) represent the background. In Fig. 2, the templates in the first row are rectilinear templates in four directions, i.e., in the directions 0°, 45°, 90°, and 135° from the horizontal axis, the second-row templates are curvilinear shapes of broken lines along the horizontal axis, the third-row templates are broken lines along the vertical axis, the fourth-row templates are curvilinear shapes with right angles oriented to the four quadrants, and the last-row templates are U-bend shapes in four directions.

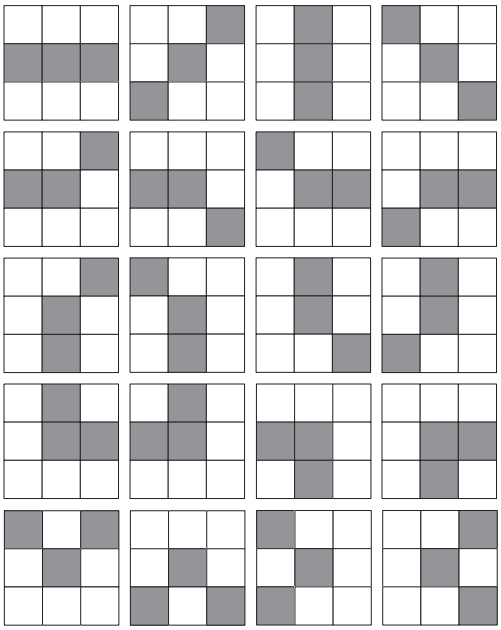

Fig. 2. Linear templates with 3 × 3 pixels.

2) Linear Template Matching: Template matching is an extensively used a technique that is in image processing to find targets in images. Standard correlation matching is a widely used template matching technique that we use in this study [36]. To find the optimal template for the considered L-object within a mixed pixel, the matching method considers the correlation coefficient between a template and a local subset of an image, which is defined as

$$r_{jk}=\frac{\sum_{m=-1}^{1}\sum_{n=-1}^{1}T_k(m,n)\cdot F_{jc}(x+m,y+n)}{\sqrt{\sum_{m=-1}^{1}\sum_{n=-1}^{1}T_k(m,n)^2\cdot\sum_{m=-1}^{1}\sum_{n=-1}^{1}F_{jc}(x+m,y+n)^2}} \tag{5}$$

where (x, y) are the coordinates of the current pixel j in the cth fraction image F_c, and $T_k(m, n)$ is the element of the kth template T_k. The closer r_{jk} is to 1, the better the kth template matches that fraction image in a local window. We view the template with the highest r_{jk} as the optimal template.

3) SPM for L-Objects: The previous two steps determine the optimal template for an L-object within a mixed pixel. This is used next to predict the spatial distribution of its subpixels. To combine the coordinates of pixels, templates, and subpixels into a unified coordinate system for facilitating following calculations, we first define a new coordinate system as follows.

1) We take the origin with coordinates (0, 0) in the upper left corner of a mixed pixel, as shown in Fig. 3.
2) The length of the mixed pixel is set equal to 1. Therefore, the coordinates of the lower right corner of the pixel are (1, 1).
3) Taking the length of the optimal template equal to that of the current mixed pixel, the new coordinates of the pixels in the templates are calculated by

$$\begin{cases} m'=\frac{2\times(m+2)-1}{6} \\ n'=\frac{2\times(n+2)-1}{6} \end{cases}, \qquad m,n=-1,0,1. \tag{6}$$

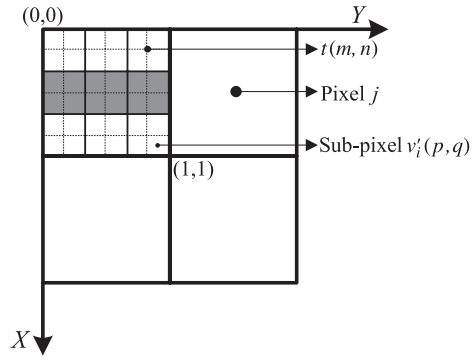

Fig. 3. Unified coordinate system for mapping L-objects.

4) The new coordinates of subpixels are then calculated using

$$\begin{cases} p'=\frac{2\times p-1}{2\times S} \\ q'=\frac{2\times q-1}{2\times S} \end{cases}, \qquad p,q=1,2,\ldots,S. \tag{7}$$

Based on this new coordinate system, SPM for L-objects involves the following four steps.

- For each mixed pixel in $\boldsymbol{V}_c^L$, the optimal template T_k of the L-objects is identified using correlation matching.
- The shortest Euclidean distance between any subpixel v_i' and each element that has the value 1 in the optimum template T_k is calculated using

$$d\left(v_i',T_k\right)=\min\left(\sqrt{\left(v_i'(p')-m'\right)^2+\left(v_i'(q')-n'\right)^2}\right). \tag{8}$$

- The shortest distances of all subpixels within the current mixed pixel are sorted in ascending order.
- According to the ascending list of subpixels, the first $F_{jc}\times S^2$ subpixels in the list are allocated to the land cover class c. This assigns the land cover class to each subpixel to the closest optimal template. $F_{jc}\times S^2$ is the fraction constraint in (2), and it determines the number of subpixels in pixel j for land cover class c.

C. SPM for A-Objects (SPM_V)

Since the introduction of SPM, there has been a proliferation of methods that assume spatial dependence [1]. Meanwhile, several studies reported a good performance of SPM by including spatial dependence when applied to A-objects [14], [24], [25], [37]. In this paper, SPM_S deals with A-objects in a similar way.

SPM_V [15] is an improvement on the geometric SPM algorithm [14], using spatial dependence when predicting the spatial distribution of A-objects. SPM_V first geometrically partitions a mixed pixel using polygons by a vector boundary extraction model. Second, a ray-crossing algorithm assigns land cover classes to subpixels within each vector boundary [15]. It consists of the following four main steps.

- For each mixed pixel in $\boldsymbol{V}_c^A$, the length and location of each segment along the boundary of the mixed pixel are estimated for all classes using the vector boundary extraction model [15].

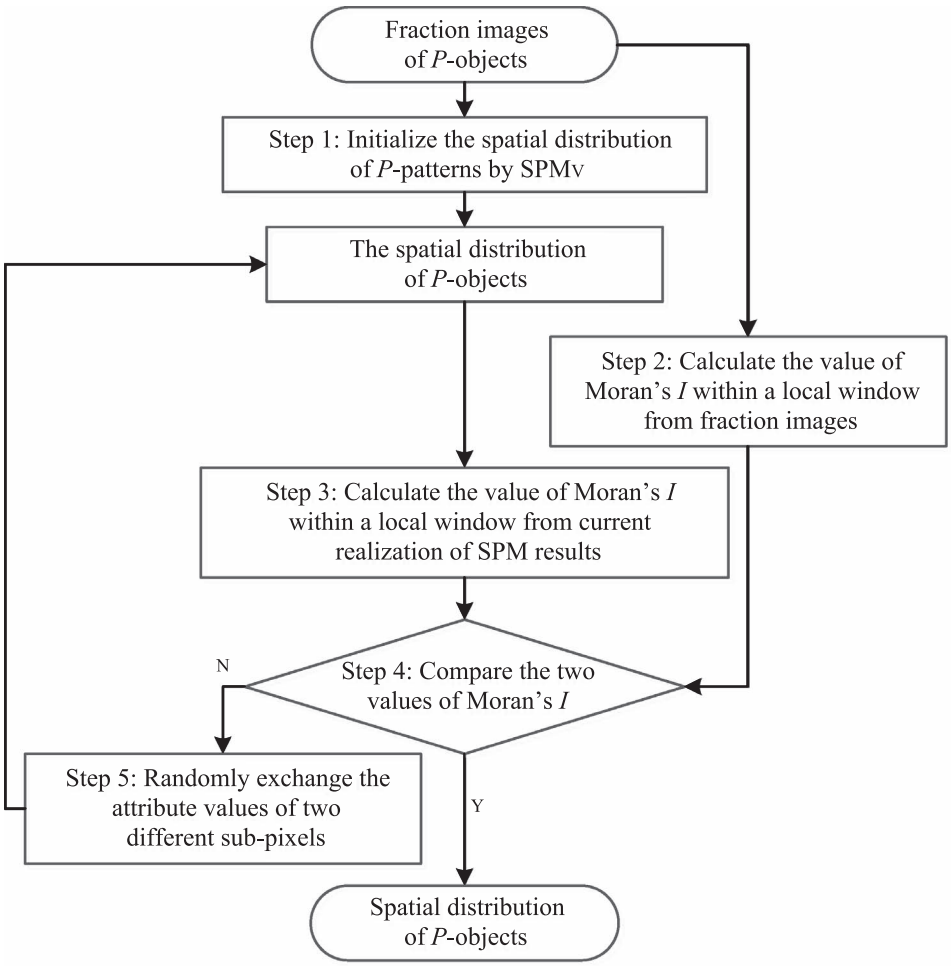

Fig. 4. Flowchart of SPM_{SP} for P-objects.

- According to these estimated segments, the initial polygons for all land cover classes within the mixed pixel are connected in the counterclockwise direction.
- These initial polygons are further adjusted to remove coincident vertices and segments to generate the final vector boundaries $\{B_c|c = 1, 2, \ldots, C\}$ of all the A-objects in a mixed pixel.
- According to the vector boundaries, the attribute values of the subpixels of each vector boundary are determined using the ray-crossing algorithm [15].

D. SPM for P-Objects (SPM_{SP})

SPM_{SP} was developed for P-objects to achieve different types of spatial point patterns: dispersed, random, and clustered. P-objects are typically much smaller than a pixel and follow either a dispersed, random, or clustered pattern. Moran's I is a popular index that describes the spatial autocorrelation (or spatial patterns) of lattice objects [38], [39]. By considering pixels in remote sensing images as lattice data, subpixels of geographical objects (such as the P-objects) are also considered as lattice data. Moran's I is used to characterize the spatial correlation of fraction images, i.e., to determine the mapping order of land cover classes in the pixel-swapping algorithm [40] and the visiting order when allocating classes using soft-then-hard SPM [41]. Therefore, Moran's I characterizes the spatial patterns of P-objects in fraction images and in SPM results. The spatial patterns of P-objects vary spatially, and thus, the value of Moran's I is computed in a local window. We have used a window size of 3×3 pixels, as recommended in [42]. The implementation of SPM_{SP} involves the following steps and is shows in Fig. 4.

- The spatial distribution of all subpixels of P-objects in $\boldsymbol{V}_c^P$ is initialized using SPM_{V} applied to fraction images.
- For each mixed pixel in $\boldsymbol{V}_c^P$, the target value of Moran's I for the cth class (i.e., I_c) in a local window of the fraction image is determined as

$$I_c = \frac{M \sum_{j=1}^{M} \sum_{j'=1}^{M} w_{jj'}(F_{jc} - \overline{F}_c)(F_{j'c} - \overline{F}_c)}{\left(\sum_{j=1}^{M} \sum_{j'=1}^{M} w_{jj'}\right) \sum_{j=1}^{M} \left(F_{jc} - \overline{F}_c\right)^2} \tag{9}$$

$$w_{jj'} = \begin{cases} 1, & \text{if } j \text{ and } j' \text{ are neighbors} \\ 0, & \text{otherwise} \end{cases} \tag{10}$$

where F_{jc} is the fraction value of class c in mixed pixel j, $\overline{F_c}$ is the mean of all fraction values of class c in a local window, and M is the number of pixels in the local window of fraction images.

- Moran's I for the cth class (i.e., I'_c) in the current SPM realization is determined as

$$I'_c = \frac{N \sum_{i=1}^{N} \sum_{i'=1}^{N} w_{ii'}(x_{ic} - \overline{x}_c)(x_{i'c} - \overline{x}_c)}{\left(\sum_{i=1}^{N} \sum_{i'=1}^{N} w_{ii'}\right) \sum_{i=1}^{N} (x_{ic} - \overline{x}_c)^2} \tag{11}$$

  where x_{ic} is the attribute value of class c in subpixel i, $\overline{x}_c$ is the mean of the attribute values of class c in a local window with the same spatial coverage as in Step 3, and $N = M \times S^2$ is the number of subpixels in a local window of the current SPM realization.
- The value of I_c from the fraction images is compared with I'_c from the current SPM realization. If $|I_c - I'_c| \leq 0.06$, no changes are made to this mixed pixel, and the next mixed pixel that contains P-objects is considered. Otherwise, we proceed to the next step.
- We randomly exchange the attribute values of two different subpixels within the mixed pixel to change the spatial distribution of P-objects after applying SPM. This way, the results become consistent with the spatial pattern in the fraction images.
- The previous three steps are repeated until either a maximum number of iterations is reached or no further swaps are made.

E. Integration

After obtaining the spatial distributions of the three patterns' objects, this step integrates these results to obtain an SPM map. To preserve the connectivity of the L-objects and the various spatial distribution patterns of the P-objects while maximizing the spatial dependence of the A-objects, we first consider A-objects as the background and overlay this with P-objects, followed by overlaying with L-objects. During integration, a land cover class may not be assigned to those subpixels to which no land cover class was assigned using the three separate SPM processes of L-, A-, and P-objects. To adjust for this, an extra step was implemented: if a subpixel is detected to be a null value by moving a window with 3×3 subpixels on the SPM map, the class is assigned that has the largest number of subpixels in a surrounding neighborhood (i.e., 3×3 subpixels) of the central subpixel.

IV. Experiments and Analysis

We used an artificial and two remotely sensed images to evaluate the performance and effectiveness of the proposed SPM_S method. It was compared with a traditional hard classifier and seven existing SPM methods: the spatial attraction model (SAM) [6], the hybrid intra- and interpixel dependence (HIIPD) [16], [43], the pixel-swapping algorithm (PSA) [2], the linearized pixel-swapping algorithm (LPSA) [30], Markov random fields (MRF) [7], [16], maximum *a posteriori* models (MAP) with a single image [19]–[21], and SPM_V. Two measurements of visual interpretation and accuracy assessment were used to validate the experimental results of the proposed method.

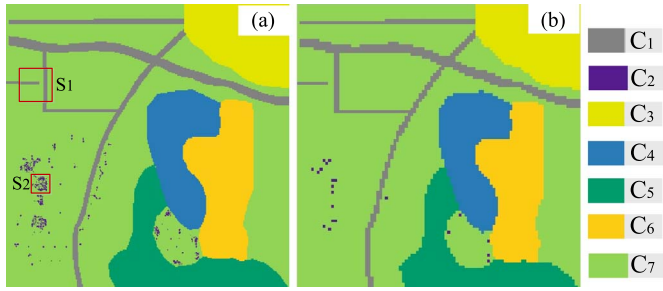

Fig. 5. Experiment using the artificial image. (a) Artificial (reference) image. (b) Hard classification ($S = 5$).

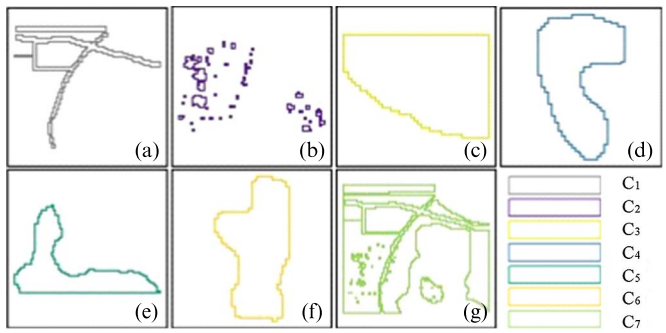

Fig. 6. Spatial objects for each land cover class of the artificial image ($S = 5$). (a) L-objects. (b) P-objects. (c)–(g) A-objects.

A. Artificial Imagery

An artificial image with 500×500 pixels was constructed to contain seven land cover classes: class C_1 of L-objects, class C_2 of P-objects, and classes C_3, C_4, C_5, C_6, and C_7 of A-objects [see Fig. 5(a)]. The artificial image in Fig. 5(a) was used as the reference image. Three scale factors of 2, 5, and 10 were considered to degrade the reference image into coarse fraction images. These coarse fraction images were taken as input for SPM methods to produce SPM maps with the same spatial resolution of the reference image by the three scale factors. A hard classification map [see Fig. 5(b)] that was obtained by hardening the fraction images ($S = 5$) was used as a benchmark for comparing the image quality of SPM maps with a hard-classified map.

1) SPM for Artificial Image: After recognition of the spatial distribution pattern, all objects were correctly recognized as L-objects [see Fig. 6(a)], P-objects [see Fig. 6(b)], and A-objects [see Fig. 6(c)–(g)], respectively. This was no surprise, because the artificial image was purposely created to test SPM_S.

Next, the determined pattern types and fraction images were input into SPM_S to obtain the spatial distribution of the subpixels for each pattern of objects. The final SPM_S result ($S = 5$) is shown in Fig. 7(h). The SPM results ($S = 5$) using SAM, HIIPD, PSA, LPSA, MRF, MAP, and SPM_V are displayed in Fig. 7(a)–(g), respectively. Fig. 7 shows no evident difference between the SPM results of A-objects. Unsmooth boundaries of L-objects appeared in Fig. 7(a)–(e) and (g), whereas smooth boundaries appeared in Fig. 7(f) and (h). The spatial distribution of P-objects in Fig. 7(a)–(g) was more clustered than that of SPM_S in Fig. 7(h). Fig. 7(f) shows that many P-objects were not preserved due to oversmoothing in MAP.

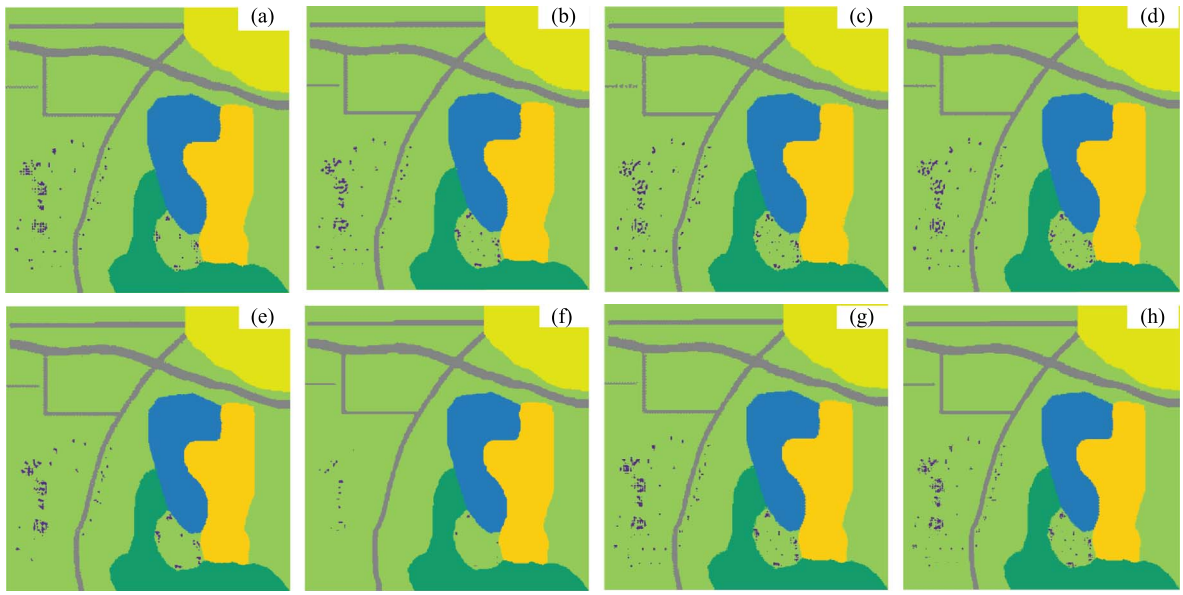

Fig. 7. SPM results ($S = 5$) for artificial image. (a) SAM. (b) HIIPD. (c) PSA. (d) LPSA. (e) MRF. (f) MAP. (g) SPM_V. (h) SPM_S.

TABLE I
OA (%) OF ARTIFICIAL IMAGE

	SAM	HIIPD	PSA	LPSA	MRF	MAP	SPM_V	SPM_S
S=2	94.51	95.58	95.41	95.80	91.80	92.83	91.08	96.73
S=5	88.16	89.39	87.53	88.24	88.29	80.19	90.48	90.58
S=10	86.03	88.07	84.30	87.25	86.26	81.35	87.06	89.73

TABLE II
OA (%) OF A-OBJECTS

	SAM	HIIPD	PSA	LPSA	MRF	MAP	SPM_V	SPM_S
S=2	92.99	93.07	93.60	93.60	86.26	92.05	92.74	92.74
S=5	92.68	92.80	91.64	91.64	92.03	84.75	92.85	92.85
S=10	91.24	92.92	91.41	91.41	92.08	81.10	91.18	91.18

2) Accuracy Assessments: For the entire image, A- and L-objects, the overall accuracy (OA) was determined to quantitatively evaluate the performance of the SPM results. Note that, in this experiment, OA was calculated as the total number of correctly classified subpixels divided by the total number of reference subpixels only within mixed pixels because fraction images generated by degrading reference images are error free [5], [13]. When considering P-objects, SPM cannot identify the absolutely accurate locations of subpixels. Therefore, we used the classified image quality in terms of visual interpretation and landscape indexes, e.g., the perimeter-area fractal dimension (PAFRAC) [44] and the aggregation index (AI) [44], to quantitatively compare the SPM_S patterns of the reference image [24]. Table I shows the OA values for three scale factors. Table I indicates that SPM_S produces the highest OA for each scale factor and it obtained increases of 2.87%, 3.11%, and 3.97% for $S = 2, 5,$ and 10, respectively, by comparing the average of the OA values from the other seven existing SPM methods.

The eight SPM methods for A-objects (see Fig. 7) produced more detailed information and better classifications than the hard classification [see Fig. 5(b)]. Table II presents the OA of A-objects (classes C_3, C_4, C_5, C_6, and C_7) and shows that the eight SPM methods produced nearly the same OA values for A-objects, except MRF with $S = 2$ and MAP with $S = 5$ and $S = 10$. Note that SPM_S used the same algorithm as SPM_V to predict the locations of A-objects and LPSA used PSA for A-objects, thus resulting in the same OA. This showed that SPM using spatial dependence is an effective solution for accurately identifying the spatial locations of A-objects.

Fig. 7(a)–(e) and (g) shows that some spatial locations of L-objects were incorrectly predicted by SPM methods, resulting in unsmooth boundaries. Connectivity of several fine L-objects was not preserved, resulting in irregular boundaries for larger L-objects, particularly for PSA. Results of the SPM_L step in SPM_S, however, indicated that the connectivity of the fine L-objects and the smoothness of the larger L-objects were effectively preserved. Results for L-objects in the subarea S_1 [marked by a red rectangle in Fig. 5(a)] are displayed in Fig. 8(a_2)–(a_9), illustrating that the result by SPM_S in Fig. 8(a_9) was closer to the reference image in Fig. 8(a_1) than those by the other seven methods, although LPSA and HIIPD produced more accurate results than SAM, PSA, MRF, MAP, and SPM_V. Although the result by MAP in Fig. 8(a_7) shows that the connectivity of fine L-objects and the smooth boundaries of large L-objects were preserved, the result was oversmoothing, and the width of L-objects was smaller than that of the reference image in Fig. 8(a_1). Table III shows that SPM_S produced the highest OA for L-objects, showing an increase of 4.21%, 6.22%, and 6.36% for scale factors of 2, 5, and 10, respectively.

These large improvements were mainly due to the SPM_L step for L-objects. When traditional spatial dependence-based SPM approaches are applied to linear objects, the fine L-objects lose their connectivity, resulting in a loss of spatial dependence. Similarly, larger L-objects result in unrealistically jagged boundaries [45]. This means that the spatial dependence-based SPM yields unsmooth boundaries for the larger L-objects, as shown in Fig. 8. In contrast, SPM_S first recognizes the L-objects from fraction images and then uses the SPM_L algorithm to find

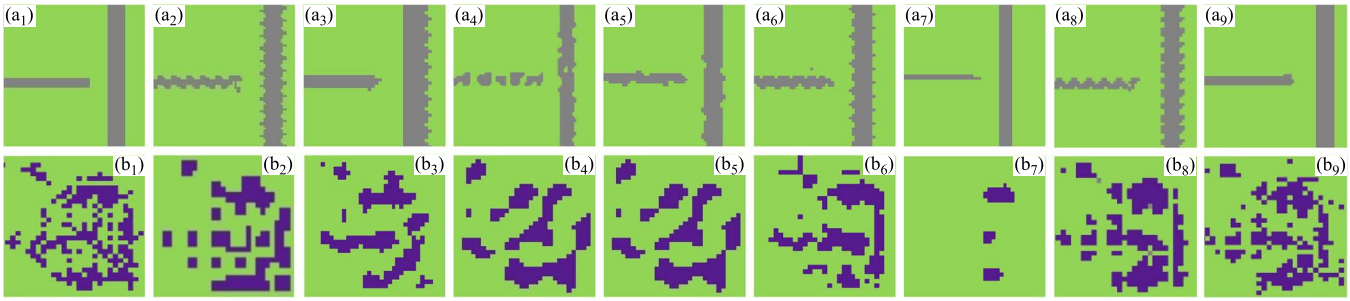

Fig. 8. SPM results ($S = 5$) for L-objects in the subarea S_1 and P-objects in the subarea S_2. (a_1)–(a_9) Reference image, SAM, HIIPD, PSA, LPSA, MRF, MAP, SPM_V, and SPM_S results in the subarea S_1, respectively. (b_1)–(b_9) Reference image, SAM, HIIPD, PSA, LPSA, MRF, MAP, SPM_V, and SPM_S results in the subarea S_2, respectively.

TABLE III
OA (%) OF L-OBJECTS

	SAM	HIIPD	PSA	LPSA	MRF	MAP	SPM_V	SPM_S
S=2	94.63	96.33	95.79	97.25	93.65	92.38	89.17	98.38
S=5	89.12	92.69	89.54	93.38	92.20	79.77	88.60	95.55
S=10	83.36	85.26	78.23	85.51	80.98	76.26	84.50	88.37

TABLE IV
ACCURACY ASSESSMENT OF P-OBJECTS

	Artificial image	S	SAM	HIIPD	PSA	LPSA	MRF	MAP	SPM_V	SPM_S
PAFRAC	1.53	2	1.50	1.37	1.42	1.42	1.38	1.50	1.43	1.55
		5	1.20	1.28	1.31	1.31	1.36	1.21	1.28	1.44
		10	1.08	1.20	1.16	1.16	1.34	1	1.32	1.46
AI	56.18	2	55.15	63.74	62.83	62.83	77.20	68.78	65.97	59.30
		5	66.77	70.38	71.51	71.51	71.25	68.59	67.66	58.37
		10	72.72	74.37	74.95	74.95	81.84	100.00	65.18	56.81

the optimal direction of the current L-objects according to the linear templates, followed by prediction of the locations of the L-objects. These linear templates play a key role in preserving the connectivity of the fine L-objects and in producing smooth boundaries for the larger L-objects. The linear templates are thus regarded as a new constraint when mapping L-objects. In this experiment, LPSA was slightly more accurate than HIIPD for L-objects, whereas SPM_S obtained an average increase of 2.05% compared with LPSA for the three scale factors. This is likely due to the fact that more templates were used in SPM_S, which can deal with more various L-objects, including linear and curvilinear cases, than LPSA. These improvements for L-objects indicated that SPM_L in SPM_S provides a solution for accurately predicting the spatial distribution of fine and large L-objects.

The class C_2 contained P-objects. Fig. 5(b) shows that most of those were lost when applying the hard classification, whereas Fig. 7(a)–(h) shows that the SPM methods retained at least some of the information. The P-objects using SPM_{SP} were more similar to the reference image compared with the other seven methods that produced more clustered P-objects. The results in subarea S_2 [marked by the red rectangle in Fig. 5(a)] are shown in Fig. 8(b_2)–(b_9). They indicate that the SPM_{SP} algorithm resulted in a spatial distribution of P-objects that was more similar to the reference image when compared with the SAM, HIIPD, PSA, LPSA, MRF, MAP, and SPM_V results. Note that, due to LPSA, utilizing the PSA algorithm to handle P-objects, results for P-objects in Fig. 8(b_4) and (b_5) are the same. MAP resulted into oversmoothing and hence into a loss in P-objects [see Fig. 8(b_7)].

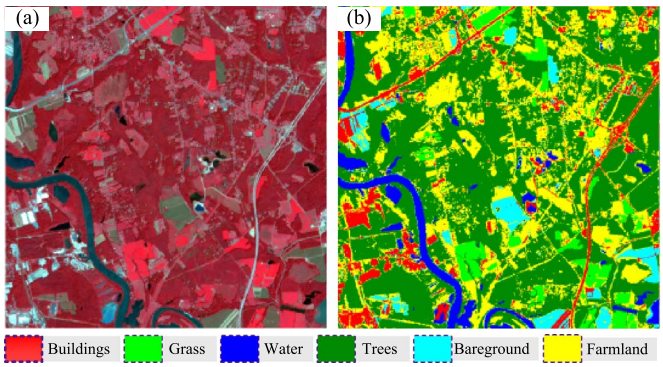

Fig. 9. Synthetic remotely sensed images. (a) ASTER pseudocolor composition imagery. (b) Hard classification map of (a).

PAFRAC and AI indexes were used to quantitatively evaluate the accuracy of P-objects. PAFRAC describes the patch shape complexity, taking values between 1 and 2, with an increasing patch shape complexity with increasing PAFRAC value. AI characterizes how patches aggregate or disaggregate in the landscape [46], taking values in the range $[0, 100]$. $AI = 0$ indicates that the patch types are maximally disaggregated, whereas $AI = 100$ indicates maximal aggregation. We have used these indexes to evaluate the performance of SPM_{SP} for P-objects and compare it with the spatial dependence-based methods (see Table IV). For scale factors equal to 2, 5, and

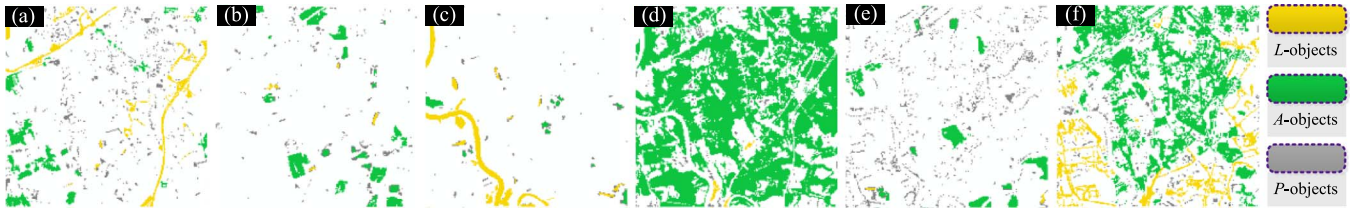

Fig. 10. Spatial patterns of each land cover class of ASTER image ($S = 3$). (a) Buildings. (b) Grass. (c) Water. (d) Trees. (e) Bare Ground. (f) Farmland.

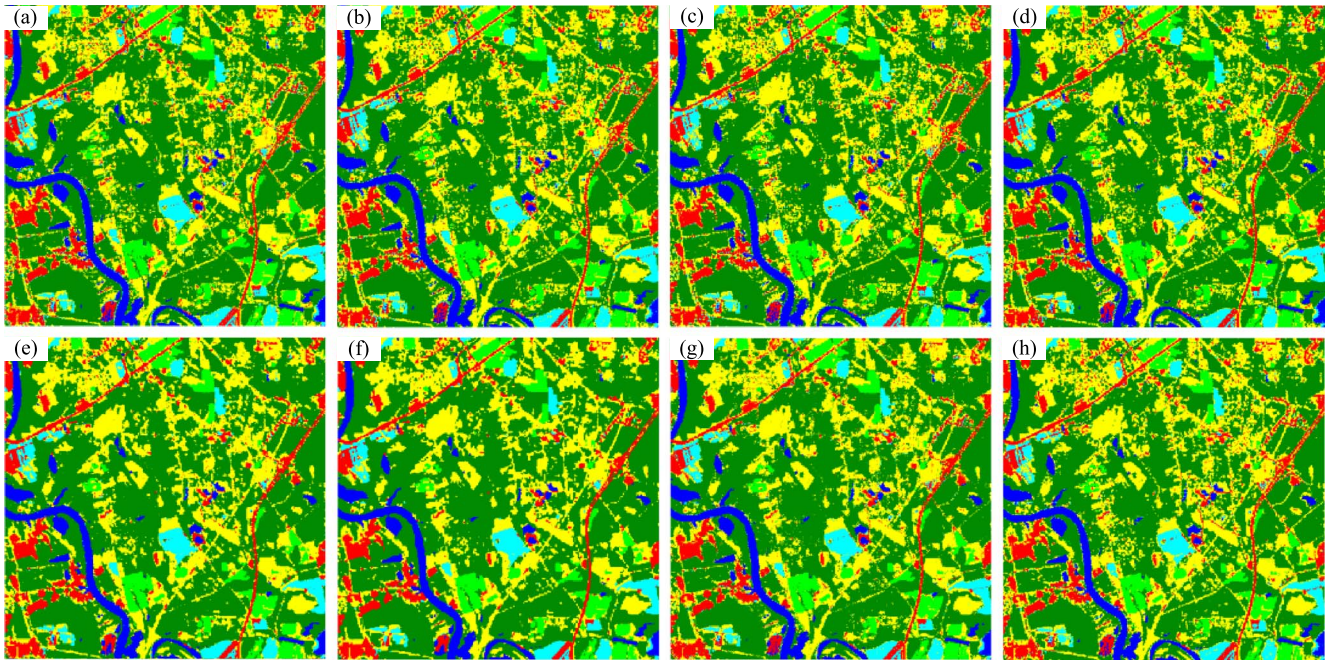

Fig. 11. SPM results ($S = 3$) for synthetic remotely sensed images. (a) SAM. (b) HIIPD. (c) PSA. (d) LPSA. (e) MRF (f) MAP. (g) SPM_V. (h) SPM_S.

10, absolute PAFRAC differences between the reference image and SPM_S were equal to 0.02, 0.09, and 0.07; average absolute PAFRAC differences between the reference image and the other seven methods were equal to 0.10, 0.25, and 0.35; absolute AI differences between the reference image and SPM_S were equal to 3.12, 2.19, and 0.63; and the average absolute AI differences between the reference image and the other seven methods were equal to 9.03, 13.48, and 21.53, respectively. The PAFRAC results indicate that the patch shape complexity of the P-objects from SPM_S was closer to the reference image, whereas the AI results indicate that aggregation of P-objects from SPM_S was closer to the reference image. The two indexes in Table IV imply that SPM methods based on spatial dependence obtain a more clustered distribution of P-objects, whereas SPM_SP results in patterns closer to the reference image. This is mainly because SPM_S uses Moran's I to characterize spatial patterns when predicting the spatial distribution of P-objects.

B. Synthetic Remotely Sensed Image

We next tested SPM methods on a 15-m multispectral Advanced Spaceborne Thermal Emission and Reflection Radiometer (ASTER) image (600 × 600 pixels), as shown in Fig. 9(a). Six main land cover classes, including buildings, grass, water, trees, bare ground, and farmland, are considered as endmembers for classification, SPM, and validation. Training samples of each endmember were manually selected from the image in Fig. 9(a) for hard classification. Fig. 9(b) shows the hard classification map by a support vector machine (SVM) [32], and it is used as the reference image for the validation of SPM results. Two scale factors $S = 3$ and $S = 6$ were tested. By applying the two scale factors, the ASTER image in Fig. 9(a) was first disaggregated into coarse remote sensing images; soft classification was then performed on these coarse images to obtain the fraction images, which were finally used as inputs of SPM methods.

1) SPM for the ASTER Image: SPM_S first recognized the P-, L-, and A-objects from each coarse fraction image, and the recognition results for $S = 3$ are shown in Fig. 10. It shows that A-objects are mainly in the classes trees and farmland, whereas L-objects appear in the classes buildings, grass, water, and farmland. Classes buildings and bare ground contain many P-objects. Recognition results and fraction images were then used as inputs to SPM_S to obtain the SPM maps. The SPM results ($S = 3$) using SAM, HIIPD, PSA, LPSA, MRF, MAP, SPM_V, and SPM_S are displayed in Fig. 11(a)–(h), respectively.

2) Accuracy Assessments: Table V presents the accuracy assessment of SPM results for the entire ASTER image and each class and shows that SPM_S produced the greatest OA for each scale factor. It can be found from Table V that it

TABLE V
ACCURACY ASSESSMENT OF THE ASTER IMAGE

S		SAM	HIIPD	PSA	LPSA	MRF	MAP	SPM_V	SPM_S
3	Buildings	77.83	79.89	78.36	79.22	79.54	79.97	79.99	90.00
	Grass	90.46	91.75	90.80	91.47	91.31	90.21	91.18	93.51
	Water	93.90	94.49	93.87	94.26	94.57	94.55	93.50	95.07
	Trees	92.89	93.68	93.18	93.44	94.39	94.57	91.56	87.11
	Bareground	77.65	78.72	77.67	78.26	73.91	72.85	83.50	83.12
	Farmland	80.29	82.37	81.20	81.78	81.00	80.90	80.59	85.79
	OA	87.71	88.96	88.15	88.58	88.68	88.68	87.66	89.41
6	Buildings	64.77	67.66	63.06	67.00	68.33	64.63	66.49	73.57
	Grass	83.42	85.40	82.28	84.56	84.88	83.71	82.73	88.30
	Water	88.22	89.83	86.31	89.33	89.16	87.17	86.88	90.92
	Trees	87.63	88.67	86.73	88.42	89.51	91.29	86.64	83.75
	Bareground	68.02	69.30	66.64	68.89	68.35	65.69	69.67	75.96
	Farmland	69.72	71.99	68.31	71.54	70.57	66.74	69.91	73.80
	OA	80.21	81.79	79.03	81.41	81.75	81.13	79.98	82.22

Fig. 12. Real remotely sensed images. (a) TM pseudocolor composition imagery. (b) High-resolution DigitalGlobe image for validation.

achieved increases of 1.06% and 1.46% for $S = 3$ and $S = 6$, respectively, by comparing the average of OA values from the other seven SPM results. The accuracy of each class in SPM_S maps was above 83% for $S = 3$ and 73% for $S = 6$. Compared with the average accuracy of each class by the existing seven SPM methods, classes buildings, grass, water, bare ground, and farmland in the SPM_S result, respectively, increased by 10.74%, 2.48%, 0.91%, 5.61%, and 4.63% for $S = 3$ and by 7.57%, 4.45%, 2.79%, 7.88%, and 3.97% for $S = 6$. Classes buildings, bare ground, and farmland had significant improvements as they contained a lot of L- and P-objects, as shown in Fig. 11.

C. Real Remotely Sensed Image

We finally tested SPM_S on a Landsat TM 5 imagery (400 × 400 pixels) in Fig. 12(a) with a spatial resolution of 30 m, acquired on August 17, 2010. A high-resolution reference image (DigitalGlobe image) acquired on August 20, 2011, covering the same area, was taken from Google Earth with a resampled spatial resolution of 6 m [see Fig. 12(b)]. Four main land cover classes, namely, vegetation, water, road, and buildings, are observed in the high-resolution reference image and are considered as endmembers for classification, SPM, and validation. Representative pixels of each endmember were manually selected from the image. To compare the performance of SPMS with that of the seven existing SPM methods, we applied a classification of SVM to generate hard and soft classification results.

1) Hard and Soft Classifications: Representative pixels for vegetation, water, road, and buildings were used as input to the hard and soft classifiers. The hard classification result using SVM is shown in Fig. 15(a), and the soft classification results of the fraction images are displayed in Fig. 13. They show that the classes vegetation and water take a large part of the study area, whereas the classes road and building account for a smaller proportion.

2) SPM for the TM Image: With $S = 5$, the seven SPM methods (SAM, HIIPD, PSA, LPSA, MRF, MAP, and SPM_V) produced the finer land cover maps in Fig. 15(b)–(h). The proposed SPM_S method first recognized the P-, L-, and A-objects from each fraction image, as shown in Fig. 14. P-, L-, and A-objects were almost correctly recognized. Recognition results show that A-objects are mainly in the classes vegetation and water. L-objects evidently appear in the class road. Classes vegetation and road, however, contain many P-objects, and the class building has a few A- and L-objects. Pattern recognition results and fraction images were then used as inputs to SPM_S to individually determine the locations of P-, L-, and A-objects, followed by their integration into the fine land cover map shown in Fig. 15(i).

3) Accuracy Assessments: One thousand eight hundred validation sites were randomly selected from the high-resolution reference image [see Fig. 12(b)]. These validation sites were first visually interpreted into land cover classes using prior knowledge of this study area. Next, they were compared with the hard classification and the different SPM methods by determining confusion matrices and statistical indexes. OA and the accuracy of each class were derived from each confusion matrix.

Table VI lists the OA and the accuracy of each class for the hard classifier of SVM and the eight SPM methods. It shows that the eight SPM methods were more accurate than the hard classifier (SVM). Specifically, the OA of SAM, HIIPD, PSA, LPSA, MRF, MAP, SPM_V, and SPM_S was 3%, 5.61%, 3.06%, 5.39%, 5%, 6.61%, 4.56%, and 10.84% higher than the OA of SVM, respectively. The SPM methods generated more accurate and detailed land cover maps at the subpixel scale. SPM_S had the highest OA equal to 84.17%, and its OA was 7.84%, 5.23%, 7.78%, 5.45%, 5.84%, 4.23%, and 6.28% higher than the OA of SAM, HIIPD, PSA, LPSA, MRF, MAP,

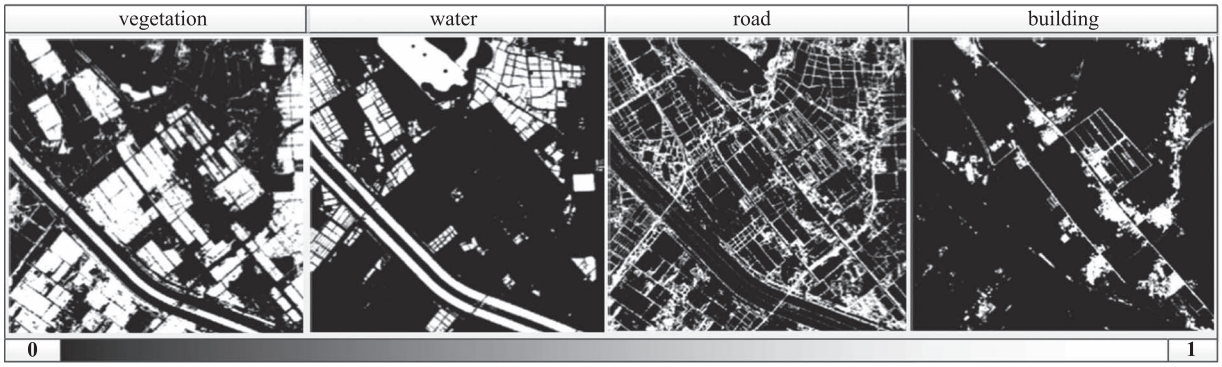

Fig. 13. Soft classification results of the TM image.

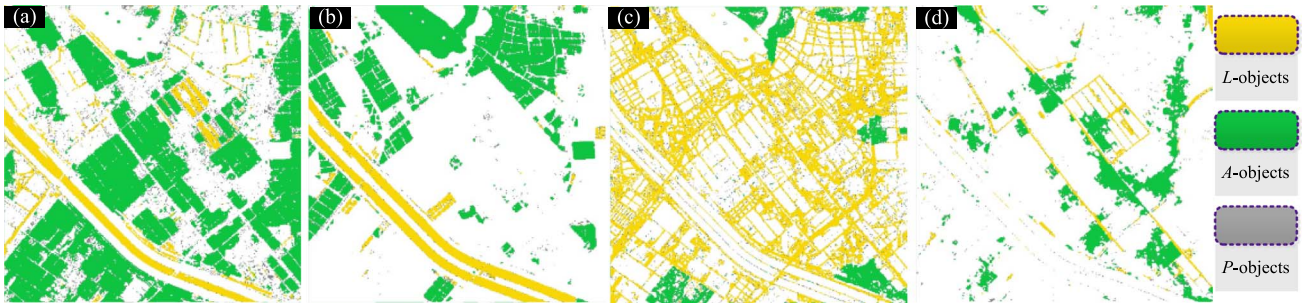

Fig. 14. Spatial patterns of each land cover class. (a) Vegetation. (b) Water. (c) Road. (d) Building.

and SPM_V, respectively. In particular, for the classes roads and buildings, which contained the most L- and P-objects according to the pattern recognition results, OA increased by 12.92% and 14.89% compared with the average OA values for each class in the seven SPM results. The main improvements in OA were due to L- and P-objects being significantly enhanced by the SPM_L and SPM_SP algorithms incorporated into SPM_S.

V. Discussion

A. Analysis of Scale Factor S

The performance of SPM with different scale factors were analyzed for the artificial image and the synthetic remote sensing image as the scale factor strongly affects the accuracy of SPM maps [24], [29], [41], [47]. Three scale factors $S = 2$, $S = 5$, and $S = 10$ were tested on the artificial image, and two scale factors $S = 3$ and $S = 6$ were tested on the synthetic ASTER image for the purpose of evaluating the performance and accuracy of SPM methods at various subpixel scales. Tables I and V show that the accuracy of the seven existing SPM methods gradually decreased as the scale factor increased. Similar to the seven SPM methods, the accuracy of the proposed SPM_S in this paper also decreased with an increased scale factor. As the scale increased, the OA of artificial image decreased by about 8%, and the OA of the synthetic ASTER image decrease by about 7%. The possible reason was that the SPM process became more complicated with the increase of scale factor and the uncertainty increased for SPM because more spatial locations of subpixels within mixed pixels needed to be predicted [5], [13].

B. Comparison of SPM Methods

When comparing SPM methods for different images, we found that the accuracy of MRF and MAP was lower than those of the other five traditional SPM methods SAM, HIIPD, PSA, LPSA, and SPM_V in several scales for the artificial image. The OA of MRF was lower than those of the other methods when using $S = 2$ for A-objects, whereas the OA of MAP was lower than those of other methods when using $S = 5$ or $S = 10$ for A- and L-objects on the entire image. This was likely because MRF usually produced overly smooth results as it did not guarantee the constraint of fraction image when predicting the spatial distribution of subpixels [7]–[10], [16], [41], [48] and MAP also did not maintain the fraction constraint as it used the winner-take-all strategy for class allocation [5], [20]. For the accuracy of the synthetic ASTER image and the TM image in Tables V and VI, the OA of MRF and MAP was almost identical with those of the other five traditional SPM methods SAM, HIIPD, PSA, LPSA, and SPM_V. In particular, the OA of MAP was slightly greater than those of SAM, HIIPD, PSA, LPSA, and SPM_V. This was largely due to that MRF and MAP can avoid some errors from soft classification with the winner-take-all strategy for class allocation [5], [20]. An interesting finding is that the winner-take-all strategy for class allocation in SPM produces slightly more accurate results than traditional class allocation algorithms using the fraction constraints [5], [41] (e.g., units of subpixel and highest attribute values first) for real remote sensing images, whereas it may generate slightly less accurate SPM maps than class allocation algorithms with fraction constraint for the downscaled error-free fraction images. Therefore, the winner-take-all strategy in SPM was an

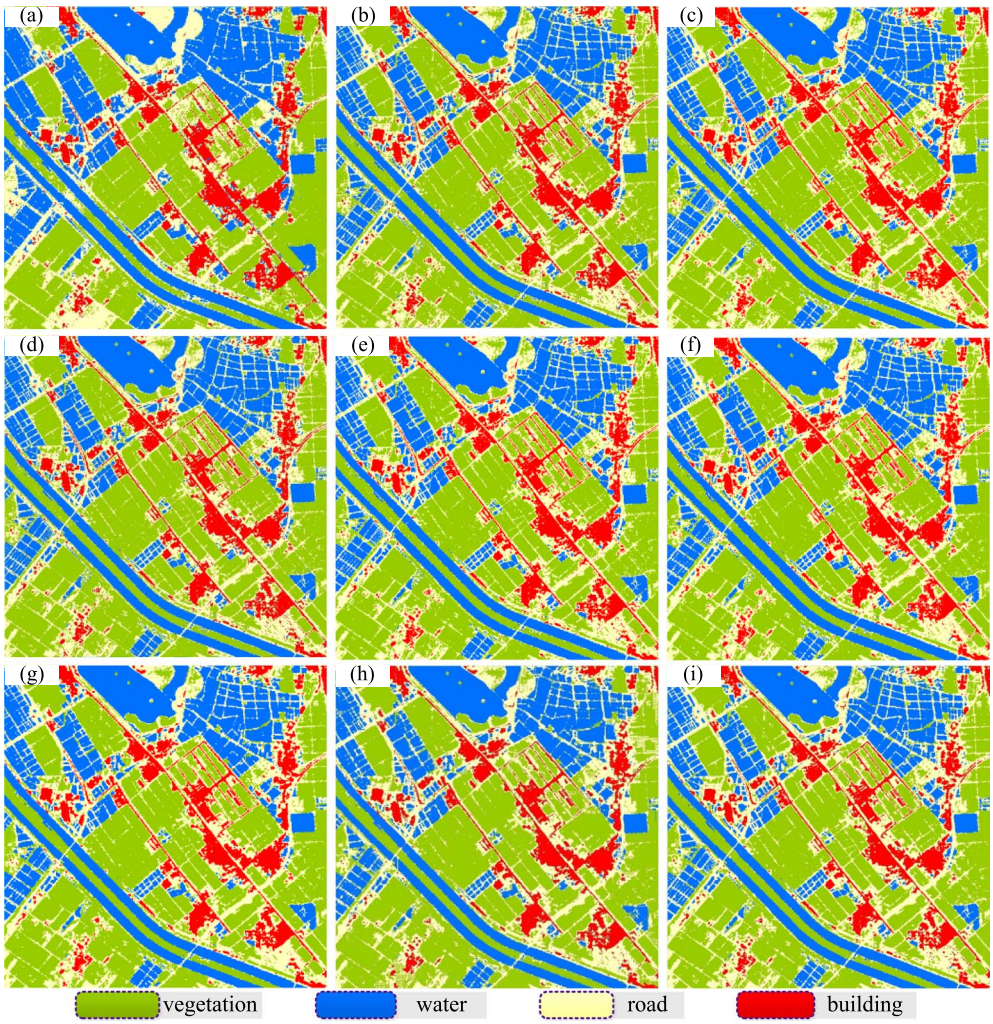

Fig. 15. SPM results for the TM image. (a) SVM. (b) SAM. (c) HIIPD. (d) PSA. (e) LPSA. (f) MRF. (g) MAP. (h) SPM_V. (i) SPM_S.

TABLE VI
ACCURACY ASSESSMENT OF TM IMAGE ($S = 5$)

	SVM	SAM	HIIPD	PSA	LPSA	MRF	MAP	SPM_V	SPM_S
Vegetation	84.89	84.36	85.96	85.16	85.43	86.10	87.03	85.29	83.29
Water	82.41	86.18	75.63	75.38	76.38	79.90	81.91	89.45	89.95
Road	58.97	63.32	75.00	61.41	73.91	67.12	71.20	60.60	80.43
Buildings	48.95	58.39	70.28	74.13	70.63	70.28	69.93	64.69	83.22
OA	73.33	76.33	78.94	76.39	78.72	78.33	79.94	77.89	84.17

effective solution to avoid some errors from soft classification of real remote sensing images in practical applications [20].

HIIPD and LPSA were slightly more accurate than SAM, PSA, and SPM_V. In particular, HIIPD generated more accurate results of A-objects, whereas LPSA produced more accurate results of L-objects. The reason was that HIIPD used both pixel- and subpixel-level spatial dependence, whereas SAM, PSA, and SPM_V used either pixel-level or subpixel-level spatial dependence [4], [43], and that LPSA improved the PSA with anisotropic exponential distance decay model [30]. Moreover, similar performances of HIIPD and LPSA on A- and L-objects were determined on the synthetic ASTER image and the real TM image. Although HIIPD and LPSA were more accurate than the other five methods, the proposed SPM_S was the most accurate one among the eight SPM methods in the three experiments. Note that the spatial distribution prediction of A-objects can be also done with any of the SPM methods under spatial dependence, such as HIIPD, MRF, and MAP. In that case, SPM_S would produce more accurate results as it produced slightly higher accuracy than SPM_V for A-objects in most cases.

C. Sensitivity Analysis for SPM_S

During the implementation of SPM_S, the weight of shape index is important to determinate the spatial pattern of objects, and the threshold of Moran's I also plays a crucial role in the iterative process of predicting the spatial distribution of P-objects. Sensitive analysis of the shape index weight and the Moran's I threshold was performed to evaluate their impacts on the accuracy of SPM_S results.

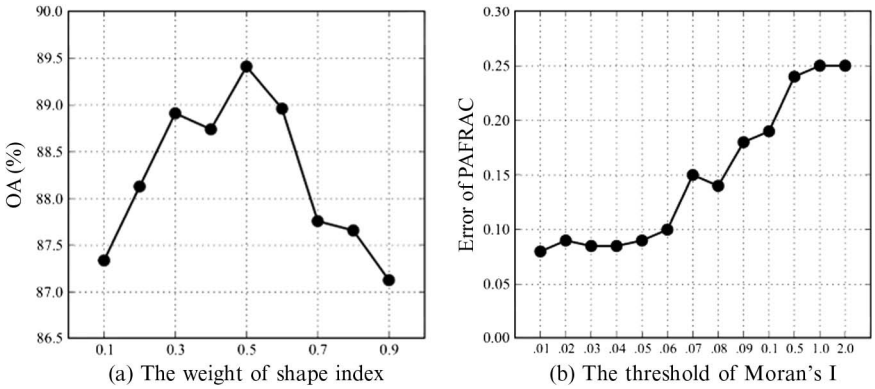

Fig. 16. Sensitivity analysis of the parameters. (a) Weight of shape index for the synthetic ASTER image ($S = 3$). (b) Threshold of Moran's I for the artificial image ($S = 5$).

Fig. 16(a) shows changes in OA with different shape index weights for the synthetic ASTER image using $S = 3$. It shows that the OA fluctuated between 87% and 89.5%. The weights between 0.4 and 0.6 achieved slightly greater OA than the other weights, and the OA reached the highest at the equal weight for the shape index and the density index. It implies that shape index and density index may have the same impact on the final SPM results. Fig. 16(b) presents the PAFRAC error between the reference image and the SPM_S results changes with different Moran's I thresholds for P-objects in the artificial image using the scale factor of 5. It shows that the thresholds between 0.5 and 2 almost led to no changes for the spatial distribution of P-objects as the threshold is too large. When the threshold was less than 0.5, particularly below 0.06, the error of PAFRAC declined greatly to be minimized and become stable. It indicates that a relatively smaller threshold may result in a similar spatial pattern of P-objects to that in the fraction images.

D. Computational Complexity Analysis for SPM Methods

For the fixed input coarse pixels n, land cover classes c, scale factor S, the number of iterations k, and the local window size w used for calculating memberships of each subpixel to classes, the worst case scenario [49] is considered in analyzing the computational complexity of the eight compared SPM methods. SAM contains two main processes: calculating attractions and allocating land cover classes to subpixels. When calculating attractions, the number of instructions depends upon the number of coarse pixels n, the number of land cover classes c, the number of subpixels within each pixel S^2, and the local window size w. Thus, the computational complexity is equal to $O(n \cdot w \cdot c \cdot S^2)$. When allocating land cover classes to subpixels in SAM, the complexity also depends upon sorting all attractions within each pixel. If the sorting process is a Quicksort algorithm, the computational complexity for the second SAM process is equal to $O(n \cdot c^2 S^4)$. By combining these two processes, the complexity of SAM is seen to be equal to $O(n \cdot \max(wcS^2, c^2 S^4))$. PSA is an iterative method and has a main process to maximize the attractiveness scores by swapping the land cover classes of two subpixels, and its complexity is thus equal to $O(k \cdot n \cdot c \cdot w \cdot S^2)$. Compared with PSA, LPSA has an extra process to find the preferred anisotropic model for each pixel before applying PSA, but the complexity of the extra process is far below that than that of PSA. Therefore, the complexity of LPSA is similar to that of PSA and is equal to $O(k \cdot n \cdot c \cdot w \cdot S^2)$, once more according to the worst case scenario. HIIPD as an iterative method that combines the pixel- and subpixel-level attractions. The main difference between HIIPD and PSA is that PSA only considers the subpixel-level attraction, whereas HIIPD considers both pixel- and subpixel-level attractions. The complexity of HIIPD is thus equal to $O(k \cdot n \cdot c \cdot w \cdot S^4)$. MRF has the prior energy function and the conditional energy function as its two main functions. The prior energy function is obtained iteratively, whereas the conditional energy function is to be calculated once from the spectral values of the original remote sensing images. The complexity of MRF is thus equal to $O(k \cdot n \cdot c \cdot w \cdot S^2)$. The complexity of MAP is associated with calculating the data fidelity term and the prior term, and its complexity is therefore equal to $O(k \cdot n \cdot c \cdot w \cdot S^2)$. SPM_V first determines the polygons of classes within each pixel, with a complexity equal to $O(n \cdot c \cdot w)$. Next, SPM_V allocates the land cover classes of subpixels, with a complexity equal to $O(n \cdot S^2)$. Combining these two steps, the complexity of SPM_V is equal to $O(n \cdot \max(cw, S^2))$. Finally, SPM_S uses three algorithms to determine the land cover classes for A-, L-, and P-objects, respectively. For A-objects, SPM_V is used, whereas for L-objects, the complexity is equal to $O(n \cdot c \cdot S^4)$, and for P-objects, it is equal to $O(k \cdot n \cdot c \cdot w^2 \cdot S^4)$. If an entire image only contains P-objects, therefore, in the worst case, the complexity of the proposed SPM_S is equal to $O(k \cdot n \cdot c \cdot w^2 \cdot S^4)$. The proportion of P-objects in real applications, however, is usually below 5% in an entire image. Therefore, the complexity of the proposed SPM_S is close to the complexity of SPM_V or the complexity of SPM_L.

VI. Conclusion

This paper has proposed a new strategy (SPM_S) for SPM. It aimed to separately recreate the spatial distribution of three different patterns (linear pattern, area pattern, and point pattern) of geographical objects. In SPM_S, we used SPM_V to maximize the spatial dependence of area pattern objects, developed SPM_L to deal with linear pattern objects, and proposed SPM_SP for point pattern objects. We used three experiments to demonstrate that SPM_S can achieve highly accurate results for A-objects. At the same time, the study shows that SPM_S is able to preserve

connectivity of fine L-objects and yield relatively smooth boundaries for larger L-objects, as compared with traditional spatial dependence-based SPM methods. Furthermore, it is able to recreate the spatial patterns of P-objects that are closer to the reference image. Hence, SPM_S is an effective solution to the SPM of objects that follow the three main spatial patterns (area pattern, linear pattern, and point pattern) in remotely sensed images.

For further research, we note that SPM_S needs to identify the spatial pattern of objects as inputs for SPM. In spatial pattern recognition of objects, the threshold of shape–density index needs to be subjectively set to distinguish between A- and L-objects. It is worthwhile to make efforts on the adaptive selection of the threshold in future research. SPM_S performs the prediction of spatial locations for A-, L-, and P-objects, respectively; and the three resulting maps are then integrated into a final SPM map. Prediction processes of each of the three patterns of objects, however, are regarded as a single objective, which, in turn, may lead to subpixels being assigned to more than one class, whereas other subpixels are not assigned to classes due to the ignorance of the relationships between the three objectives. Therefore, we plan to further formulate SPM_S as a multiobjective optimization issue in prediction of the spatial distribution of geographical objects.

ACKNOWLEDGMENT

The authors would like to thank the editor and anonymous reviewers for their valuable comments and suggestions.

REFERENCES

[1] P. M. Atkinson, "Mapping sub-pixel boundaries from remotely sensed images," in *Innovations in GIS 4*. London, U.K.: Taylor and Francis, 1997, pp. 166–180.

[2] P. M. Atkinson, "Sub-pixel target mapping from soft-classified, remotely sensed imagery," *Photogramm. Eng. Remote Sens.*, vol. 7, pp. 839–846, 2005.

[3] J. Verhoeye and R. De Wulf, "Land cover mapping at sub-pixel scales using linear optimization techniques," *Remote Sens. Environ.*, vol. 79, no. 1, pp. 96–104, Jan. 2002.

[4] Y. Chen, Y. Ge, Q. Wang, and Y. Jiang, "A subpixel mapping algorithm combining pixel-level and subpixel-level spatial dependences with binary integer programming," *Remote Sens. Lett.*, vol. 5, no. 10, pp. 902–911, 2014.

[5] Y. Chen, Y. Ge, G. B. M. Heuvelink, J. Hu, and Y. Jiang, "Hybrid constraints of pure and mixed pixels for soft-then-hard super-resolution mapping with multiple shifted images," *IEEE J. Sel. Topics Appl. Earth Obs. Remote Sens.*, vol. 8, no. 5, pp. 2040–2052, May 2015.

[6] K. C. Mertens, B. De Baets, L. P. C. Verbeke, and R. R. de Wulf, "A sub-pixel mapping algorithm based on sub-pixel/pixel spatial attraction models," *Int. J. Remote Sens.*, vol. 27, no. 15, pp. 3293–3310, 2006.

[7] T. Kasetkasem, M. K. Arora, and P. K. Varshney, "Super-resolution land cover mapping using a Markov random field based approach," *Remote Sens. Environ.*, vol. 96, no. 3/4, pp. 302–314, Jun. 2005.

[8] X. Li, Y. Du, and F. Ling, "Spatially adaptive smoothing parameter selection for Markov random field based sub-pixel mapping of remotely sensed images," *Int. J. Remote Sens.*, vol. 33, no. 24, pp. 7886–7901, 2012.

[9] V. A. Tolpekin and A. Stein, "Quantification of the effects of land-cover-class spectral separability on the accuracy of Markov-random-field-based superresolution mapping," *IEEE Trans. Geosci. Remote Sens.*, vol. 47, no. 9, pp. 3283–3297, Sep. 2009.

[10] L. G. Wang and Q. M. Wang, "Subpixel mapping using Markov random field with multiple spectral constraints from subpixel shifted remote sensing images," *IEEE Geosci. Remote Sens. Lett.*, vol. 10, no. 3, pp. 598–602, May 2013.

[11] A. Boucher and P. C. Kyriakidis, "Super-resolution land cover mapping with indicator geostatistics," *Remote Sens. Environ.*, vol. 104, no. 3, pp. 264–282, Oct. 2006.

[12] Q. Wang, P. M. Atkinson, and W. Shi, "Indicator cokriging-based subpixel mapping without prior spatial structure information," *IEEE Trans. Geosci. Remote Sens.*, vol. 53, no. 1, pp. 309–323, Jan. 2015.

[13] Q. Wang, W. Shi, and L. Wang, "Indicator cokriging-based subpixel land cover mapping with shifted images," *IEEE J. Sel. Topics Appl. Earth Obs. Remote Sens.*, vol. 7, no. 1, pp. 327–339, Jan. 2014.

[14] Y. Ge, S. Li, and V. C. Lakhan, "Development and testing of a subpixel mapping algorithm," *IEEE Trans. Geosci. Remote Sens.*, vol. 47, no. 7, pp. 2155–2164, Jul. 2009.

[15] Y. Ge, Y. Chen, S. Li, and Y. Jiang, "Vectorial boundary-based subpixel mapping method for remote-sensing imagery," *Int. J. Remote Sens.*, vol. 35, no. 5, pp. 1756–1768, 2014.

[16] J. Hu, Y. Ge, Y. Chen, and D. Li, "Super-resolution land cover mapping based on multiscale spatial regularization," *IEEE J. Sel. Topics Appl. Earth Obs. Remote Sens.*, vol. 8, no. 5, pp. 2031–2039, May 2015.

[17] F. Ling, X. Li, F. Xiao, and Y. Du, "Superresolution land cover mapping using spatial regularization," *IEEE Trans. Geosci. Remote Sens.*, vol. 52, no. 7, pp. 4424–4439, Jul. 2014.

[18] X. Xu, Y. Zhong, and L. Zhang, "Adaptive subpixel mapping based on a multiagent system for remote-sensing imagery," *IEEE Trans. Geosci. Remote Sens.*, vol. 52, no. 2, pp. 787–804, Feb. 2014.

[19] X. Xu, Y. Zhong, L. Zhang, and Z. Hongyan, "Sub-pixel mapping based on a MAP model with multiple shifted hyperspectral imagery," *IEEE J. Sel. Topics Appl. Earth Obs. Remote Sens.*, vol. 6, no. 2, pp. 580–593, Apr. 2013.

[20] Y. Zhong, Y. Wu, X. Xu, and L. Zhang, "An adaptive subpixel mapping method based on MAP model and class determination strategy for hyperspectral remote sensing imagery," *IEEE Trans. Geosci. Remote Sens.*, vol. 53, no. 3, pp. 1411–1426, Mar. 2015.

[21] Y. Zhong, Y. Wu, L. Zhang, and X. Xu, "Adaptive MAP sub-pixel mapping model based on regularization curve for multiple shifted hyperspectral imagery," *ISPRS J. Photogramm. Remote Sens.*, vol. 96, pp. 134–148, Oct. 2014.

[22] Y. F. Zhong, and L. P. Zhang, "Remote sensing image subpixel mapping based on adaptive differential evolution," *IEEE Trans. Syst., Man, Cybern. B, Cybern.*, vol. 42, no. 5, pp. 1306–1329, Oct. 2012.

[23] Y. F. Zhong and L. P. Zhang, "Sub-pixel mapping based on artificial immune systems for remote sensing imagery," *Pattern Recognit.*, vol. 46, no. 11, pp. 2902–2926, Nov. 2013.

[24] P. M. Atkinson, "Issues of uncertainty in super-resolution mapping and their implications for the design of an inter-comparison study," *Int. J. Remote Sens.*, vol. 30, no. 20, pp. 5293–5308, 2009.

[25] P. M. Atkinson, "Downscaling in remote sensing," *Int. J. Appl. Earth Obs. Geoinf.*, vol. 22, pp. 106–114, Jun. 2013.

[26] A. M. Lechner, A. Stein, S. D. Jones, and J. G. Ferwerda, "Remote sensing of small and linear features: Quantifying the effects of patch size and length, grid position and detectability on land cover mapping," *Remote Sens. Environ.*, vol. 113, no. 10, pp. 2194–2204, Oct. 2009.

[27] A. J. Tatem, H. G. Lewis, P. M. Atkinson, and M. S. Nixon, "Super-resolution land cover pattern prediction using a Hopfield neural network," *Remote Sens. Environ.*, vol. 79, no. 1, pp. 1–14, Jan. 2002.

[28] P. M. Atkinson, "Super-resolution land cover classification using the two-point histogram," in *geoENV IV-Geostatistics for Environmental Applications*. Dordrecht, The Netherlands: Springer-Verlag, 2004, pp. 15–28.

[29] B. Ai, X. Liu, G. Hu, and X. Li, "Improved sub-pixel mapping method coupling spatial dependence with directivity and connectivity," *IEEE J. Sel. Topics Appl. Earth Obs. Remote Sens.*, vol. 7, no. 12, pp. 4887–4896, Dec. 2014.

[30] M. W. Thornton, P. M. Atkinson, and D. A. Holland, "A linearised pixel-swapping method for mapping rural linear land cover features from fine spatial resolution remotely sensed imagery," *Comput. Geosci.*, vol. 33, no. 10, pp. 1261–1272, Oct. 2007.

[31] K. T. Chang, *Introduction to Geographic Information Systems*, 7th ed. New York, NY, USA: McGraw-Hill, 2014.

[32] M. Song and D. Civco, "Road extraction using SVM and image segmentation," *Photogramm. Eng. Remote Sens.*, vol. 70, no. 12, pp. 1365–1371, 2004.

[33] N. Mat-Isa, M. Mashor, and N. Othman, "Seeded region growing features extraction algorithm; its potential use in improving screening for cervical cancer," *Int. J. Comput., Internet Manag.*, vol. 13, no. 1, pp. 61–70, 2005.

[34] C. E. Woodcock and A. H. Strahler, "The factor of scale in remote sensing," *Remote Sens. Environ.*, vol. 21, no. 3, pp. 311–332, Apr. 1987.

[35] T. Blaschke, "Object based image analysis for remote sensing," *ISPRS J. Photogramm. Remote Sens.*, vol. 65, no. 1, pp. 2–16, Jan. 2010.
[36] L. Ding, A. Goshtasby, and M. Satter, "Volume image registration by template matching," *Image Vis. Comput.*, vol. 19, no. 12, pp. 821–832, 2001.
[37] Y. Ge, "Sub-pixel land-cover mapping with improved fraction images upon multiple-point simulation," *Int. J. Appl. Earth Obs. Geoinf.*, vol. 22, pp. 115–126, Jun. 2013.
[38] L. Anselin, "Local indicators of spatial association—LISA," *Geograph. Anal.*, vol. 27, no. 2, pp. 93–115, Apr. 1995.
[39] H. Li and J. F. Reynolds, "On definition and quantification of heterogeneity," *Oikos*, vol. 73, no. 2, pp. 280–284, Jun. 1995.
[40] Y. Makido, A. Shortridge, and J. P. Messina, "Assessing alternatives for modeling the spatial distribution of multiple land-cover classes at sub-pixel scales," *Photogramm. Eng. Remote Sens.*, vol. 73, no. 8, pp. 935–943, 2007.
[41] Q. Wang, W. Shi, and L. Wang, "Allocating classes for soft-then-hard subpixel mapping algorithms in units of class," *IEEE Trans. Geosci. Remote Sens.*, vol. 52, no. 5, pp. 2940–2959, May 2014.
[42] Q. Wang, W. Shi, and H. Zhang, "Class allocation for soft-then-hard subpixel mapping algorithms with adaptive visiting order of classes," *IEEE Geosci. Remote Sens. Lett.*, vol. 11, no. 9, pp. 1494–1498, Sep. 2014.
[43] F. Ling, X. Li, Y. Du, and F. Xiao, "Sub-pixel mapping of remotely sensed imagery with hybrid intra- and inter-pixel dependence," *Int. J. Remote Sens.*, vol. 34, no. 1, pp. 341–357, 2013.
[44] J. Peng *et al.*, "Evaluating the effectiveness of landscape metrics in quantifying spatial patterns," *Ecol. Indicators*, vol. 10, no. 2, pp. 217–223, Mar. 2010.
[45] Y.-F. Su, G. M. Foody, A. M. Muad, and K.-S. Cheng, "Combining pixel swapping and contouring methods to enhance super-resolution mapping," *IEEE J. Sel. Topics Appl. Earth Obs. Remote Sens.*, vol. 5, no. 5, pp. 1428–1437, Oct. 2012.
[46] D. Moser *et al.*, "Landscape patch shape complexity as an effective measure for plant species richness in rural landscapes," *Landscape Ecol.*, vol. 17, no. 7, pp. 657–669, Oct. 2002.
[47] Y. Chen, Y. Ge, and D. Song, "Super-resolution land-cover mapping based on high-accuracy surface modeling," *IEEE Geosci. Remote Sens. Lett.*, vol. 12, no. 12, Dec. 2015.
[48] J. P. Ardila, V. A. Tolpekin, W. Bijker, and A. Stein, "Markov-random-field-based super-resolution mapping for identification of urban trees in VHR images," *J. Photogramm. Remote Sens.*, vol. 66, no. 6, pp. 762–775, Nov. 2011.
[49] C. H. Papadimitriou, *Computational Complexity*. Hoboken, NJ, USA: Wiley, 2003.

Yong Ge (M'14) received the Ph.D. degree in cartography and geographical information system from the Chinese Academy of Sciences (CAS), Beijing, China, in 2001.

She is currently a Professor with the State Key Laboratory of Resources and Environmental Information System, Institute of Geographical Sciences and Natural Resources Research, CAS. She is also currently with the Jiangsu Center for Collaborative Innovation in Geographical Information Resource Development and Application, Nanjing, China. She has directed research in over ten national projects. She has authored or coauthored over 100 scientific papers published in refereed journals, one book, and six chapters in books and has edited one book. She is the holder of five granted patents in improving the accuracy of information extraction from remotely sensed imagery. Her research activity focuses on spatial data analysis and data quality assessment.

Dr. Ge has been involved in the organization of several international conferences and workshops. She is a member of the Theory and Methodology Committee of the Geographic Information Society, the International Association of Mathematical Geosciences, and the Editorial Board of Spatial Statistics (Elsevier).

Yuehong Chen received the B.S. degree in geographical information system from Hohai University, Nanjing, China, in 2010, and the M.S. degree in cartography and geographical information system from the University of Chinese Academy of Sciences, Beijing, China, in 2013. He is currently working toward the Ph.D. degree in the State Key Laboratory of Resources and Environmental Information System, Institute of Geographical Sciences and Natural Resources Research, Chinese Academy of Sciences, Beijing.

His current research interests focus on remote sensing image processing and superresolution mapping.

Alfred Stein was born in 1958. He received the M.Sc. degree in mathematics and information science, with a specialization in applied statistics, from Eindhoven University of Technology, Eindhoven, The Netherlands, and the Ph.D. degree, from Wageningen University, Wageningen, The Netherlands, in 1991, on spatial interpolation.

He started his career as an Assistant Professor with the Department of Soil Science and Geology, Wageningen University. In 1995, he was appointed as a Visiting Professor at the ITC International Institute of Geo-information Science and Earth Observation, which was then an independent research institute. In 2002, he became a Professor of spatial statistics and image analysis at the new Department of Earth Observation Science, which he headed for over ten years. In 2008, he became a Vice-Rector for Research of the institute, a position that he held for four years. After the merge of ITC with the University of Twente in 2010, he continued to be a member of the faculty management team. He is a member of the SENSE Research School. Since 1998, he has successfully supervised over 30 Ph.D. students on a range of spatial (and spatio/temporal) statistical topics. His research interests focus on statistical aspects of spatial and spatiotemporal data in the widest sense.

Dr. Stein has been the Editor-in-Chief of *Spatial Statistics*, the new leading platform in the field of spatial statistics, since 2011.

Sanping Li received the Ph.D. degree in computer engineering from the University of Massachusetts Lowell, Lowell, MA, USA, in 2012.

He is currently an Associate Principal Research Scientist with the Office of the CTO and EMC Labs China, EMC Corporation, Beijing, China. His current research interests include subpixel mapping methods for remote sensing images, predictive analytics in the cloud and data centers with machine learning and deep learning, traffic security analytics in data centers, software-defined networking, and network function virtualization.

Jianlong Hu received the B.S. degree in information and computing science and the M.S. degree in computer application technology from Shanxi University, Taiyuan, China, in 2003 and 2006, respectively.

He is currently with the School of Computer and Information Technology, Shanxi University. His main research interests include remote sensing image analysis and machine learning.